Investigation of sulphate hydride anti-perovskite as solid electrolyte

A. Urrutia, E. Salager, P.E. Cabelguen, R. Janot, J.N. Chotard

Investigation of Sulphate Hydride Anti-perovskite as Solid Electrolyte

A.Urrutia[1,4], E. Salager[2,4], P.E. Cabelguen[3], R. Janot[1,4], J.N. Chotard[1,4]

[1] Laboratoire de Réactivité et Chimie des Solides (LRCS), Université de Picardie Jules Verne, UMR 7314 CNRS, 33 Rue Saint Leu, Amiens 80039, France

[2] Conditions Extrêmes et Matériaux : Haute Température et Irradiation (CEMHTI), UPR 3079 CNRS, Université d'Orléans, 1D Avenue de la Recherche Scientifique, Orléans 45071, France

[3] Umicore, 31 rue Marais, 1000 Brussels, Belgium

[4] Réseau sur le Stockage Electrochimique de l'Energie (RS2E), FR 3459 CNRS, 33 Rue Saint Leu, Amiens 80039, France

Abstract

Over the last decade, anti-perovskites have drawn significant attention as potential solid-electrolytes for solid-state batteries. Due to the increase in consumption of lithium, there has been a push towards next generation batteries, including sodium-ion batteries. The first representative of the material class of sulphate hydride anti-perovskites, Na_3SO_4H, was synthesized by solid-state methods as a possible electrolyte for sodium solid-state batteries. Structural characterization confirms the results reported in literature with *P*4/*nmm* space group Thermal measurements (DSC and TGA) reveal the stability of the material up to 633 K with H_2 release beginning shortly after. Here were report the first electrochemical measurements of this new sulphate hydride anti-perovskite with room temperature conductivity of 4.0 x 10^{-7} S/cm. Similarly, the electronic conductivity was also measured by Direct Current (DC) experiments to understand a non-linear Arrhenius plot of the conductivity. From the EIS and DC measurements, it is suggested that the electronic and ionic conductivities of this material fall in the same range at room temperature. Upon heating, the material becomes a mainly ionic conductor, explaining the change in the activation energy values in the Arrhenius plot (0.83 eV at low T and 0.24 eV at high T). Solid-state NMR hints at defects in the structure that correspond to Na1 and Hb-c-d dynamics.

Keywords: anti-perovskite, solid-electrolyte, conductivity, sodium, battery, X-ray diffraction

1. Introduction

Next generation energy storage devices are driven by the limitations of lithium-ion batteries. To overcome these limitations, solid-state batteries (SSBs) have been of great interest due to their potential for increased safety and higher energy density.[1] In the last decade, anti-perovskite electrolytes have drawn significant attention as solid electrolytes for use in SSBs.[2−5] Anti-perovskites are charge inverted perovskites, first reported in 1981, with a general formula X_3BA where X is a monovalent cation, ideally the mobile species, B is a divalent anion and A is a monovalent anion.[6] Similar to perovskites, the flexibility of anti-perovskite chemistry enables the design and synthesis of many different anti-perovskite compositions.[5,7−9] The majority of the publications produced for anti-perovskites have shifted towards predicting new crystal structures with high ionic conductivities through DFT calculations.[9−12]

Over the last decade, lithium-rich anti-perovskites (LiRAPs) have reported conductivities exceeding 10^{-2} S/cm[13] and electrochemical stabilities up to 9 V versus Li^+/Li.[2,14,15] Although these results are ideal for SSBs, they are rarely reproduced. Most of the LiRAPs phases are hydrated phases with the general formula $Li_{3-x}O_{1-x}H_xA$ (X: Cl, Br).[16] For all of the reported LiRAPs, conductivities vary from 2.5 x 10^{-2} S/cm down to 1.2 x 10^{-8} S/cm at room temperature.[13,17] This variance in results poses a question to their chemical and electrochemical stabilities and their possible use as ionic conductors. Besides the conductivity values, there is also significant ambiguity of the room temperature crystal structure of these LiRAPs.

Approximately three-quarters of the world's production of lithium precursors are being consumed by battery manufacturing which is up 300% in the last decade.[18,19] Lithium's popularity in portable batteries is owing to its lightweight and size. The next apparent candidate is sodium which is the sixth most abundant element in earth's crust and has driven a push towards post-lithium solid electrolytes, including β-Al_2O_3[20], NASICON[21−23] and sodium thiophosphates and the like[24,25].[26]

Recently, M_3HCh (M = Li,Na and Ch = Chalcogenides) with an ionic conductivity of 10^{-4} S/cm at 473 K reported for $Na_{2.9}HSe_{0.9}I_{0.1}$.[27,28] This brings the attention to the new family of hydride anti-perovskites with compositions Na_3AO_4X (A=S,Se X=H,F,Cl) NaRAPs have been predicted and/or synthesized with the highest conductivity (predicted) of $Na_3SO_4F_{0.5}Cl_{0.5}$ being 8.1 x 10^{-3} S/cm at 300 K.[7,27,29] Of these compositions, only two phases have been successfully synthesized, Na_3SO_4H and Na_3SO_4F, and the second one has a reported conductivity value of only 2.44 x 10^{-8} S/cm at 313 K.[7,27,29] In this work, we investigate the new sulphate hydride Na_3SO_4H anti-perovskite and focus on the electrochemical behavior of this composition as a solid electrolyte candidate for Na-ion batteries.

2. Experimental

2.1 Materials Synthesis

To synthesize Na_3SO_4H, a 1:1.1 stoichiometric ratio of dried sodium sulfate (Fisher Scientific, Na_2SO_4, anhydrous, 99+%) and sodium hydride (Sigma Aldrich, NaH dry, 90%, stored in glovebox) was used. For the doped samples, $Na_{3-2x}M_xSO_4H$ (x = 0.05, 0.2 and M: Mg, Ca), x moles of dried $MgSO_4$ and $CaSO_4$ were added stoichiometrically to partially substitute Na_2SO_4. The powders were mixed by planetary ball-milling using a Fritsch Pulverisette 7 Premium mill, 45 cc zirconia jars and 10 x 10 mm zirconia balls. The milling duration was 24 hours and the ball to powder weight ratio was of 32:1. Na_2SO_4 , $MgSO_4$, $CaSO_4$ were dried overnight and stored in an Ar filled glovebox and all synthesis was performed under Ar atmosphere due to the moisture sensitivity of the sample and precursors.[27] After milling, the powder was pressed into a 600 mg pellet (diameter = 13 mm) placed in an alumina crucible and sealed in a steel autoclave with 30 bars of H_2 pressure. The pellet was then annealed at 613 K for 12 hours under H_2 with a heating ramp of 5 K/min and cooled at approximately 0.5 K/min.

2.2 Powder X-ray diffraction

Powder X-ray diffraction of the ball-milled and annealed powders were measured using a Bruker D8 Discover diffractometer in reflection geometry with Cu radiation where $\lambda_{k\alpha1}$ = 1.54060 Å and $\lambda_{k\alpha2}$ = 1.54439 Å with a 2θ range between 10° and 50° and a 0.02° step size and 0.9 s per step. Due to the sensitivity of samples to moisture and air, the powder diffraction was performed using a homemade airtight sample holder with a Be window.[30] The unit cell parameters were refined using the LeBail fit method with the FullProf software.[31]

2.3 Thermal Analysis

Thermal measurements were performed in a glove box in a Pt-Rh+Al_2O_3 crucible using a NETZSCH STA 449 F3 thermal analyzer (TGA) coupled with differential scanning calorimetry (DSC) from 313 K to 823 K at a heating rate of 5K/min. The calorimetry measurements were also coupled with a mass spectrometer to measure any gas release.

2.4 Electrochemical Characterization

Electrochemical impedance spectroscopy (EIS) measurements were performed on 13 mm diameter pellets pressed at 5 tons in a stainless-steel die using a hydraulic oil press (i.e. Pressure = 380 MPa). The pellet's compacity was calculated by taking the density of the pellet and dividing it by the crystallographic density, resulting in a compacity of approximately 78%. The powder was pressed between 2 pieces of Papyex® (flexible graphite) foil which served as malleable contacts to the gold blocking electrodes. The pellet was then placed in a Biologic CESH cell, sealed in the glovebox under Ar atmosphere and measured using a Biologic MTZ-35 impedance analyzer between 30 MHz and 0.1 Hz with a 50-mV voltage perturbation.

The Nyquist plots were fit using ZView software. In the equivalent circuit used, a constant phase element is used in place of a capacitor due to the non-perfect nature of the capacitance of ions in the material. The first CPE1-R in parallel correspond to impedance of the bulk material and the CPE2 corresponds to the interface of the solid electrolyte with the ion blocking electrodes. The EIS measurements were performed between 298 K and 373 K.

Chrono-amperometry, direct current, (DC) measurements were performed using a Biologic VMP3-128 potentiostat between 50 mV and 250 mV with 50 mV increments and current measured at each potential for 2 h. The sample was pressed between two 10 mm stainless steel pistons inside a polyacrylate matrix at 3 tons (380 MPa). This polyacrylate assembly was placed in a homemade device and tightened with a wrench with 21 N.m of torque to maintain pressure during the DC measurements. Finally, this homemade device was sealed in an airtight jar with sealed electrical connections.

2.5 Solid-State Nuclear Magnetic Resonance Spectroscopy

Solid-state NMR measurements at room temperature were performed on Bruker Avance Neo 20 T spectrometer, Avance I 9.4 T and Avance III 4.7 T spectrometers, using Bruker 4 mm probes. Samples were packed in 4 mm outer-diameter zirconia rotor in an Ar glovebox and spun at 10 kHz under N_2 gas for all the measurements of this study. Data were Fourier transformed without apodization. For 1D spectra, baseline distortion was corrected in dmfit[32] with the spline-on-spectrum function, followed by a fit (details in SI). Shifts were referenced to aqueous NaCl (1mol.L^{-1}) at 0 ppm for ^{23}Na and pure TMS at 0 ppm for ^{1}H.

High-resolution MAS-NMR 1D spectra were recorded at 20 T. The ^{23}Na spectrum was recorded with a single pulse excitation of duration 0.7 µs at 150 W for ^{23}Na ($\pi/18$ to be quantitative). The recycling delay was 1 s for ^{23}Na and 256 transients were coadded. A single pulse of duration 3.75 µs at 100 W (67 kHz) was used for ^{1}H after 1 h polarization in the magnet, as longitudinal relaxation was very slow.

The two-dimensional ^{1}H-^{23}Na HETCOR spectrum was recorded at 9.4 T. A saturation sequence was performed, followed by a relaxation delay of 70 s for ^{1}H. The cross-polarization step lasted 1.5 ms with RF fields of 70 kHz for ^{1}H and 60 kHz for ^{23}Na. The Na dimension was recorded without ^{1}H decoupling. 48 increments were recorded in the indirect dimension with a dwell time of 100 µs. 64 transients were coadded for each increment. Experimental time ~15 h.

The ^{23}Na MQMAS spectrum was recorded in the same conditions. A short 4 µs excitation pulse was followed by an evolution delay and a 3.25 µs reconversion pulse (500 W). A short z-filter of 100 µs was applied before acquisition with a selective pulse (25 µs at a RF field of 5 kHz). The indirect dimension was recorded with 64 increments with a dwell time of 100 µs. 720 transients were coadded for each increment, with a relaxation delay of 1 s. Experimental time: ~14h.

The temperature NMR study and EXchange SpectroscopY (EXSY) experiments were performed at 4.7 T. A single pulse excitation of duration 0.419 µs at 80 W ($\pi/18$ to be quantitative) was applied for the ^{23}Na 1D spectra, with a recycling delay of 2 s and 256 or 128 scans. ^{1}H NMR data were collected using a 3.13 µs single pulse at 41.3 W (80 kHz) and the same procedure as in the paragraph above. The sensor reading is directly reported without further calibration as no obvious change was observed.

The 2D ^{23}Na-^{23}Na EXSY data were obtained at room temperature with the same setup. The recycling time was 0.8 s and 32 transients were co-added for each increment; 416 increments were recorded with a dwell time of 100 µs. No recoupling was applied during the mixing times. 2D spectra were obtained for mixing times of 100 µs, 20 ms and 200 ms (3h30 each).

3. Results and Discussion

Anti-perovskites (X_3BA) are characterized by $(BX_6)^{4+}$ octahedra within an A matrix. However, the recently reported hydride anti-perovskites Na_3SO_4H and M_3HCh (M = Li, Na and Ch = chalcogenide) inverse the A and B sites where the H^- monovalent anion sits on the B site and the chalcogen or divalent polyanion sits centered on the A site. With the H^- on the B site, $(HX_6)^{5+}$ octahedra are present. Recently, the structure of Na_3SO_4H was solved by Mutschke et al. [27] Like perovskites, the anti-perovskite structure can be characterized by the Goldschmidt factor and for Na_3SO_4H has a $\tau = 0.475$ which deviates significantly from the ideal value of 1.[33−35] It is hypothesized that the octahedral distortions resulting in a tetragonal structure accommodate the different ionic radii to stabilize the structure. Due to the high coherent scattering of hydrogen atoms, the crystal structure of Na_3SO_4H was solved using powder neutron diffraction on a deuterated sample Na_3SO_4D crystallizing in *P4/nmm* space group with a = 7.00530(5) Å and c = 4.85822(4) Å.[27]

Contrary to traditional anti-perovskites with a cubic halide framework and OX_6 octahedra, the structure of Na_3SO_4H is composed of SO_4^{2-} framework with HNa_6^{5+} octahedra (cf. **Fig. 1**a). More specifically, these octahedra are slightly distorted with the H^- sitting at an octahedral interstitial. Because of the tetragonal geometry of the SO_4^{2-} polyanion, we expect these polyanion to rotate and accommodate sodium mobility within the structure. The rotational nature of polyhedra has shown increased conductivity in other ionic conductors through the paddlewheel effect. [36]

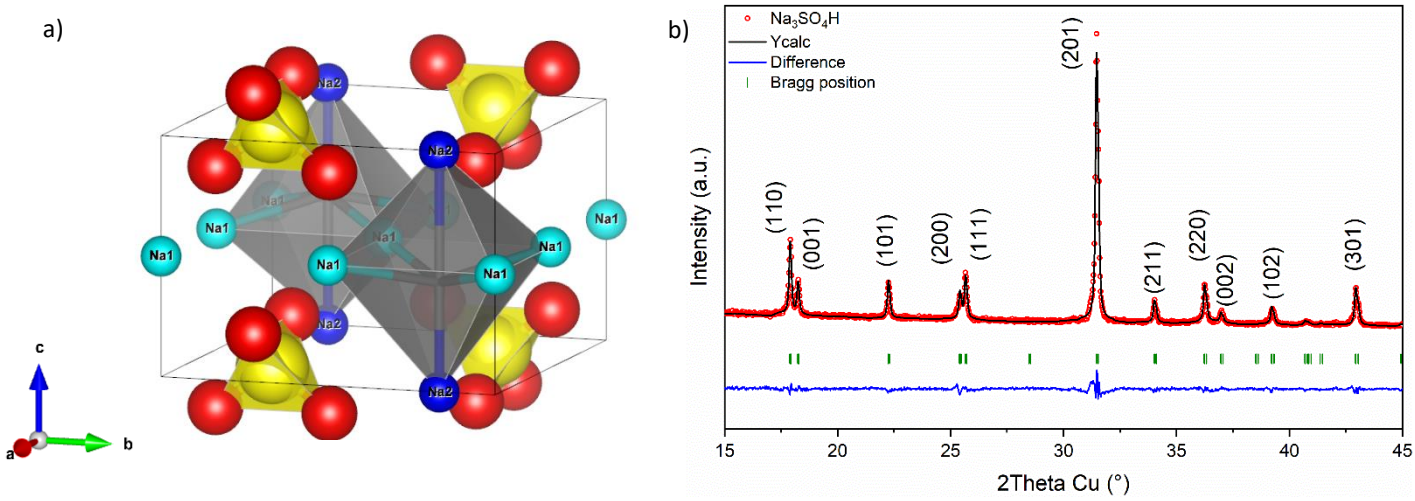

Fig. 1. a) Unit cell structure of Na_3SO_4H reproduced from crystallographic data from reference [27] with Na1 (4e) atoms in cyan and Na2 (2c) atoms in blue, H in grey (octahedral site), S in yellow, and O in red. b) LeBail fit (black line) of annealed Na_3SO_4H with experimental data in red circles, Bragg reflections in green with their corresponding (hkl) indices, and the difference plot in blue.

Studies have been performed on the different Frenkel and Schottky defects present in anti-perovskites where lattice distortions can lower activation barriers for Li^+/Na^+ motion.[8,37] Because of the orientation of the SO_4^{2-} tetrahedra, a slight distortion in the HNa_6 octahedra is observed where the H^- anion does not sit exactly at the octahedral interstitial site. Although variations from the ideal cubic anti-perovskite ($Pm\bar{3}m$) might tend to reduce the stability and increase the energy above the hull, the tetragonal Na_3SO_4H was reproduced in this work and found to be thermodynamically stable.[8,27]

Mechanochemical synthesis has shown success at synthesizing metastable phases and more specifically synthesizing anti-perovskite phases.[38–40] The diffractogram of the ball-milled (SI Figure S1) sample does not reflect a completed synthesis and shows some extra peaks that do not correspond to precursors nor the targeted Na_3SO_4H phase. The extra peaks were not attributed and disappeared after annealing at 613 K. After annealing, the synthesis of Na_3SO_4H is confirmed as shown in **Fig. 1b** with refined unit cell parameters of a = 7.00552 (19) and c = 4.85915 (25).

The DSC and thermogravimetric analysis (TGA) of the annealed sample suggests stability of the compound up to 633 K with 0.72 % mass loss up to 773 K (**Fig.**). An initial endothermic peak at 659 K with an onset temperature around 633 K corresponds to H_2 release and is confirmed by a small peak at 661 K in the mass spectra for m/Z = 2. This weight loss of 0.72 % is in rather good agreement with the H content of the Na_3SO_4H compound (0.61 wt.%). This endothermic peak is followed by an exothermic peak at 702 K which is assumed the continued exothermic release of H_2. No phase transitions or thermal events were visible between 298 K and 633 K.

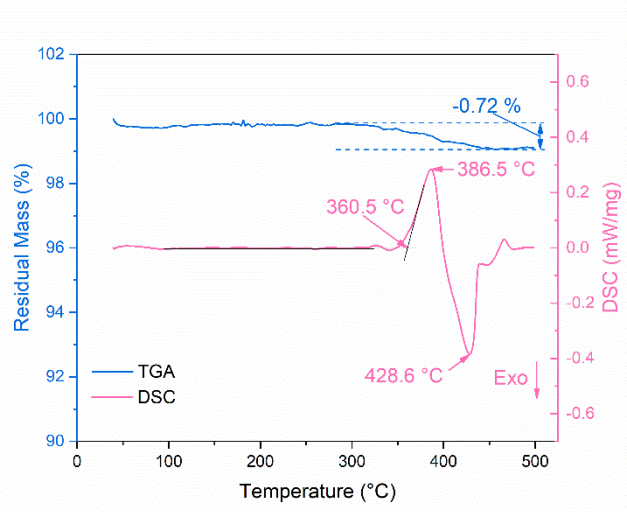

Fig. 2. TGA (blue) and DSC (pink) at 5K/min of annealed Na_3SO_4H

Following the thermal characterization of annealed Na_3SO_4H, both alternating current (AC), EIS, and direct current (DC), chrono-amperometry, measurements were performed and reported in this work for the first time. The temperature EIS measurements are summarized in **Fig.** with the Nyquist plots (a) and an Arrhenius plot of the conductivity (b) in which both the ball-milled sample (black) and the annealed sample (red) are compared. In **Fig. a**, the resistance gradually decreases with increasing temperature which is characteristic of an ionic conductor. Furthermore, the Arrhenius plot in **Fig. b** shows the ball-milled sample has a lower conductivity than the annealed sample by approximately three to four orders of magnitude at room

temperature. The room temperature conductivity is around 4.0 x 10^{-7} S/cm for annealed Na_3SO_4H and 1.0 x 10^{-10} S/cm for the ball-milled sample.

For the annealed sample, two separate linear regions are observed **Fig. b**, a high temperature region and a low temperature region, each with their own activation energies. For the low temperature region, between 298 K and 323 K, the measured activation energy is 0.83 eV. Comparing this value to a similar composition (Na_3SO_4F, E_a = 0.275 eV) reported in literature, the low temperature activation energy is three times higher.[29] Conversely, the high temperature region, between 333 K and 373 K, has an activation energy of 0.24 eV which falls close to the 0.275 eV reported for Na_3SO_4F.

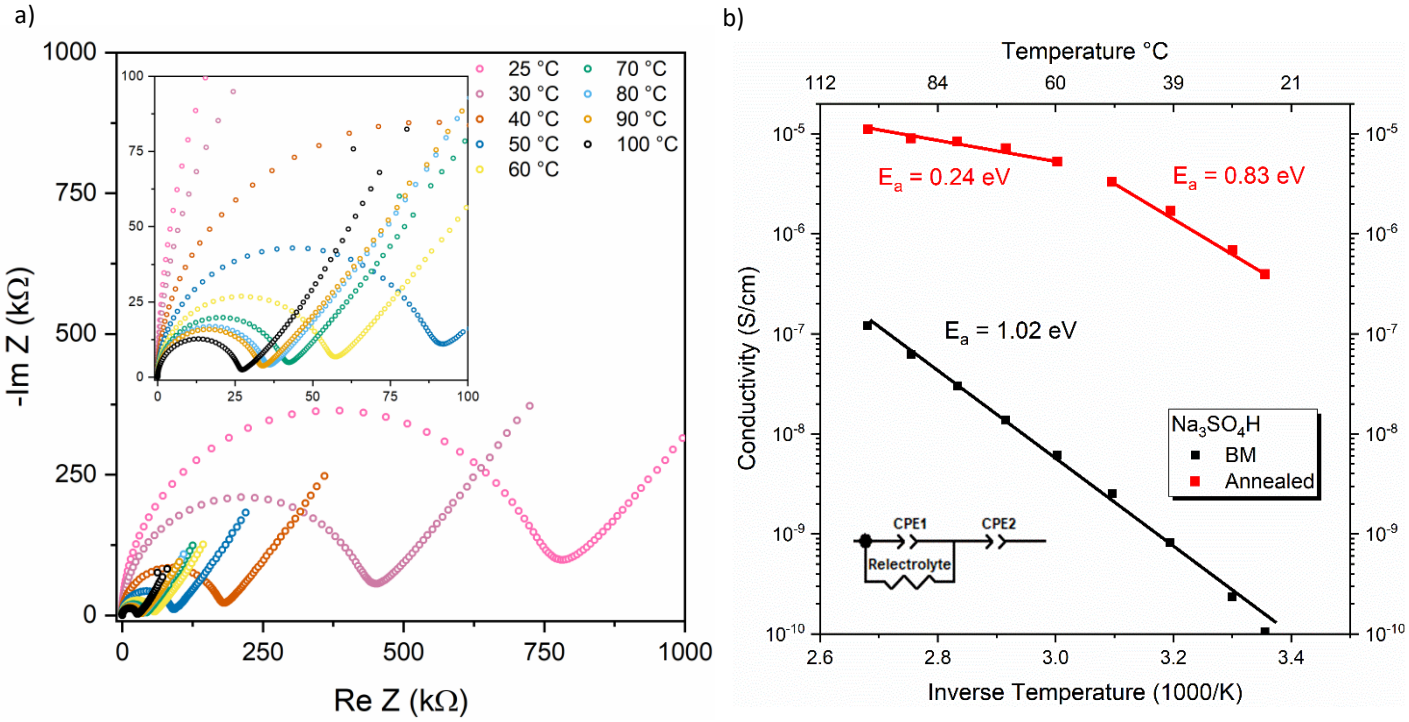

Fig. 3. a) Nyquist plots of temperature EIS measurements of annealed Na_3SO_4H with a zoom of the higher temperatures in the inset. b) Arrhenius plot of the conductivity values of Na_3SO_4H extracted from the Nyquist plots with the equivalent circuit on the bottom left, the ball-milled sample in black, and the annealed sample in red, and their respective activation energies.

This difference in activation energy is often attributed to a phase transition within the material. According to the thermal measurements, especially by DSC, there is no phase transition within this temperature range. Solid electrolytes are usually characterized by a high ionic conductivity but the electronic conductivity of solid electrolytes must also be sufficiently low to avoid self-discharge and any parasitic side reactions.[41−43] The non-linear evolution (change in activation energy) of the Arrhenius plot for the annealed Na_3SO_4H sample could be due to similar values for the ionic and electronic conductivities at lower temperatures. In order to characterize the electronic conductivity, chronoamperometry (DC) measurements were performed on the annealed sample as shown in **Fig. 4a**.

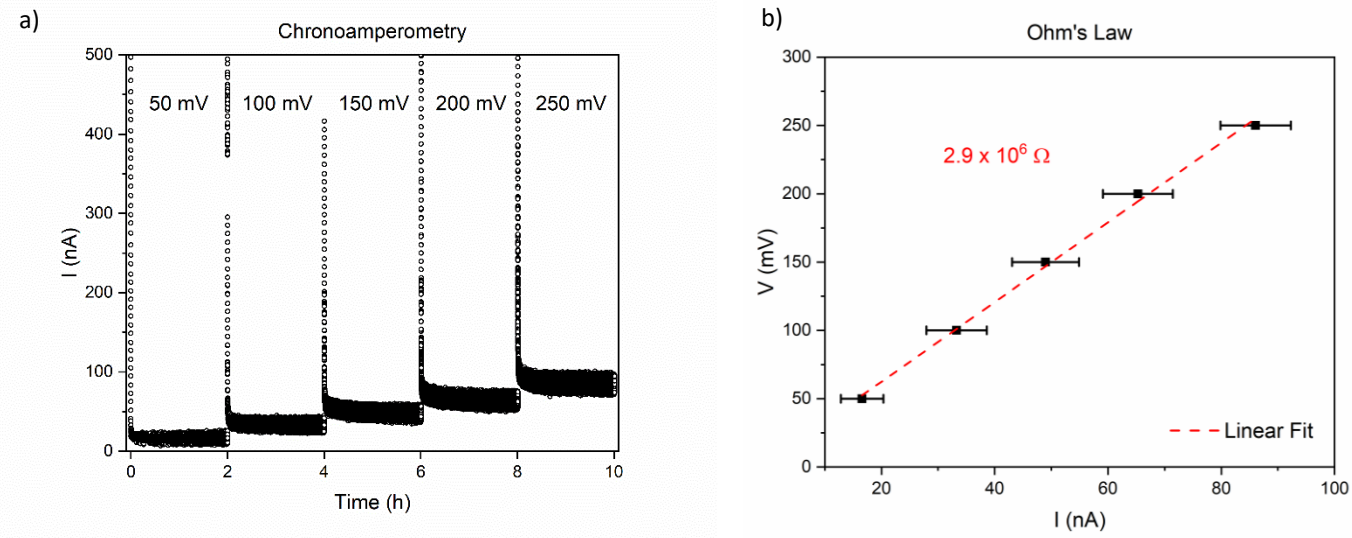

Fig. 2. Chronoamperometry (DC polarization) of annealed Na_3SO_4H (a) and relationship between V and I representing Ohm's law (b) at 298 K.

The sample was subjected to 50 mV to 250 mV potentials in 50 mV increments for 2 h each to allow for current relaxation. The electronic resistance of 2.9 MΩ at room temperature was extracted using Ohm's law (V = IR) (cf. **Fig. 4b**). This resistance corresponds to an electronic conductivity of 4.4 x 10^{-8} S/cm at room temperature. This phenomenon of mixed electronic ionic conductor creating a non-linear relationship between conductivity and temperature was also reported in Li_3OCl anti-perovskites synthesized by radiofrequency magnetron sputtering.[44] Taking a closer look at the activation energy of the annealed sample, there is a decrease in activation energy from 0.83 eV at the low temperature range to 0.24 eV at high temperatures. It is assumed that the electronic conductivity contribution is too low compared to the ionic conductivity to have a significant effect on the total conductivity. We suggest then, the change in activation energy is due to an effect of grain boundary and/or a change of defect association at low temperature (carriers trapped/untrapped at low/high temperature, respectively).

In their work [28], Mutschke *et al.* reported ^{23}Na and ^{1}H NMR measurements on Na_3SO_4H of which they identified two sodium sites in the *P*4/*nmm* tetragonal structure and two hydrogen sites of which one came from Na_3SO_4H and the other from impurities which were unidentified and unexplained by X-ray diffraction. Surprisingly, the authors reported a quadrupolar constant C_Q of 0 MHz for the Na2 (2c) site, despite the fact that the local symmetry is not isotropic (4mm symmetry). **Fig. 5a** shows the ^{23}Na Multiple Quantum Magic Angle Spinning (MQMAS) NMR measurement at 9.4 T and its fit. In good agreement with the former study, two main Na sites are found: Na1 (4e) at 5.5 ppm (C_Q = 1.41 MHz) and Na2 (2c) at 14.1 ppm (C_Q = 300 kHz). Three additional Na environments were necessary to provide a reasonable fit: Na3 next to Na1 at 4.4 ppm (C_Q = 1.74 MHz), and two environments close to Na2 (Na4 and Na5) at 12.4 ppm (C_Q = 1.02 MHz) and 12.7 ppm (C_Q = 660 kHz), respectively. The details of the fits are available in **SI**. MQMAS experiment is inherently not quantitative, so we turned to a ^{23}Na short pulse MAS-NMR 1D spectrum.

A ^{23}Na 1D spectrum was recorded at 20 T for better resolution (**Fig. 5b)** and to determine the relative amount of each crystallographic Na site and the contribution of the additional environments. A reasonable fit was obtained with the same model as that used for the MQMAS experiment (extra intensity is observed between 7 and 11 ppm, due to the excitation of the center band of satellite transitions). As expected, the lineshape of the peaks is less distorted and less shifted by quadrupolar interaction at 20 T compared to 9.4 T. The fit indicates that Na1 (4e) and Na2 (2c) contribute to 75mol% of the total signal, with a relative ratio of 61:39 (close to the expected 66:33 ratio). Three other Na environments account for 14.6mol% (Na3), 6.4mol% (Na4) and 1.6mol% (Na5) of the total Na signal. Na3 and Na4 are assigned to defective environments in Na_3SO_4H as discussed in the next paragraphs. Na5 and an extra environment (Na6 at 17.4 ppm, 2.5%, not detected in the MQMAS), are tentatively assigned to impurities.

Fig. 5c shows the ^{1}H NMR spectrum at 20 T and its fit. The peak assigned to ^{1}H(a) in Na_3SO_4H was fitted with a chemical shift of 2.9 ppm, in agreement with the previous study, and amounts to 78% of the ^{1}H signal. At least three sites were identified near -3 ppm (Hb:15.2%, Hc:6.1% and Hd:0.7%), a relatively unusual electron-rich environment for ^{1}H that was assigned to impurities by Mutschke *et al.*

The NMR spectra of the precursors were measured and do not match with these extra ^{1}H signals. So, we investigated these extra ^{1}H environments at negative shifts at 9.4 T with a ^{1}H-^{23}Na HETCOR 2D spectrum. **Fig 5**d shows, as expected, the correlation between the H(a) environment at 2.9 ppm and the two Na1(4e) and Na2(2c) crystallographic sites of Na_3SO_4H. This correlation corroborates the relatively slow dynamics of ^{1}H and ^{23}Na in the sample, which is not fast enough to average out ^{1}H and ^{23}Na heteronuclear dipolar couplings. Interestingly, the ^{1}H(c) environment at -3.9 ppm also correlates to Na1 and Na2. Another set of correlations is obtained for ^{1}H(b), with Na3 and Na4. H(d) / Na5 are not visible in the 2D-HETCOR spectrum, either because each belongs to a phase without ^{23}Na/^{1}H atoms (respectively), or because the intensity of their peak is too low. Altogether, these results prompt us to suggest that ^{1}H(c) and ^{1}H(b), Na3 and Na4 are rather signatures of H defect sites (or close to defects) in Na_3SO_4H, while ^{1}H(d) and Na5 would be impurity phases from the synthesis.

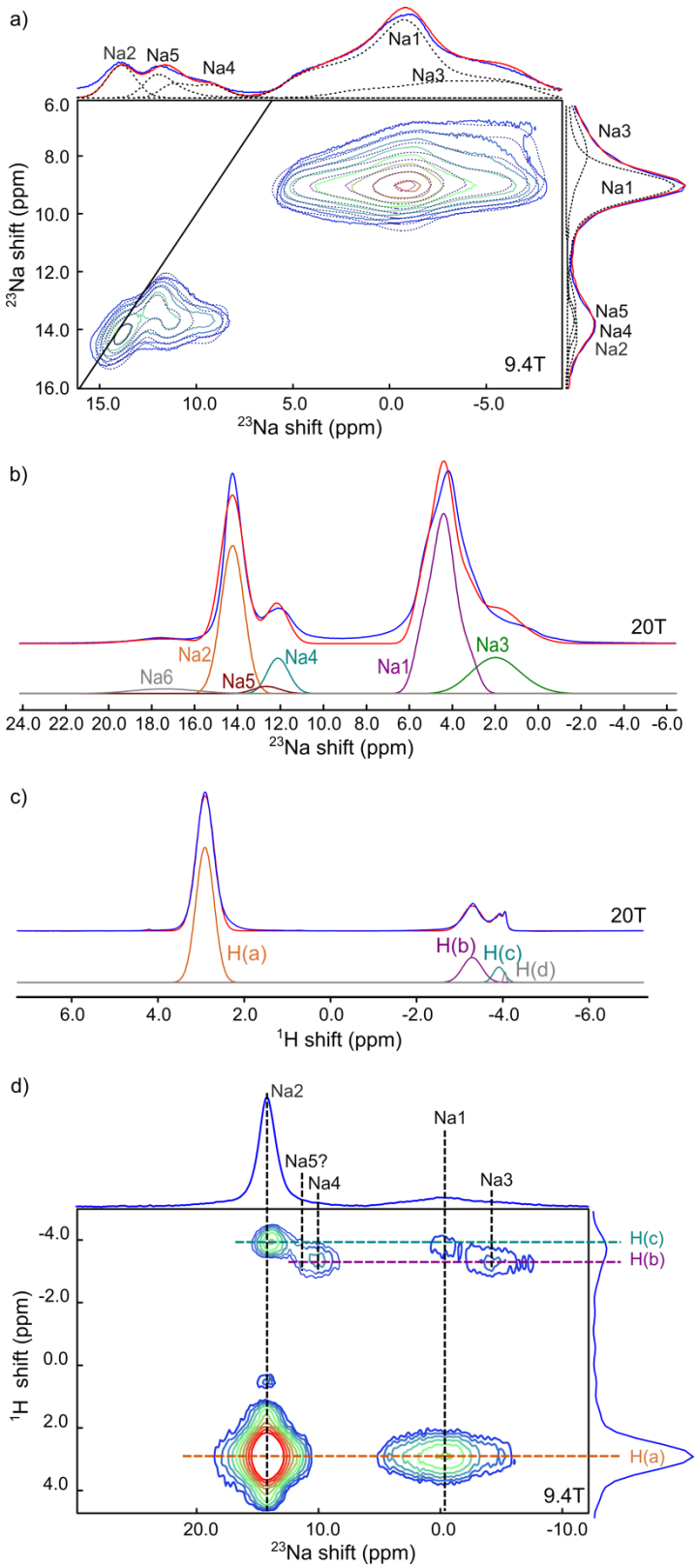

Fig. 5. (a) 9.4 T ^{23}Na MQMAS contour spectrum in plain lines and its fit in dotted lines, (b) 20 T ^{23}Na 1D spectrum, (c) 20 T ^{1}H 1D spectrum and (d) 9.4 T ^{1}H-^{23}Na HETCOR solid-state NMR spectrum of the annealed Na_3SO_4H sample.

In order to understand the ionic mobility of the hydride and sodium ions, ^{23}Na solid-state NMR spectra of the annealed Na_3SO_4H sample were measured at temperatures going from 303 K to 423 K with a dedicated WVT probe in a 4.7 T spectrometer (**SI** Fig. S5). The ^{23}Na spectra are not resolved enough at 4.7 T to constrain properly a fit with 5 contributions varying with temperature. We therefore comment qualitatively the evolution of the spectra. At room temperature, the peak maxima, assigned to the Na1 and Na2 sites, are 1750 Hz apart. Going up in temperature to 423 K, the difference between peak maxima lowers slightly to 1530 Hz, with no noticeable narrowing for Na2 but a decrease in the width in the 10 to 20 ppm region. This is most probably due to increased dynamics and is compatible with a mechanism of ionic conduction through Na1 ions and possibly Na3.

Exchange-spectroscopy (EXSY) ^{23}Na-^{23}Na measurements with mixing times up to 200 ms (**SI** Fig. S6) did not detect any exchange between the two types of Na sites at room temperature, excluding Na hoping between Na1(4e) and Na2(2c) sites as the main

ionic diffusion pathway. It is worth noting that this does not provide information about site jumps between equivalent sites (Na1-Na1 or Na2-Na2). This could be investigated through longitudinal T_1 relaxation measurements in the future.

^{1}H NMR measurements were also performed to probe changes in mobility through lineshape analysis from 303 to 423 K, but the H(a) peak in Na_3SO_4H did not show any significant change (less than 5% narrowing). The H(b-c-d) peaks, not well-resolved at 4.7 T, were fitted with a single gauss-lorentzian line. Its width narrows slightly from 1.7 ppm to 1.3 ppm, as well as the gaussian to lorentzian ratio (from 90% gaussian, to 58% gaussian and 42% lorentzian) from 303 to 423 K. These results indicate a slight increased dynamic of Hb-c-d atoms.

In this temperature range, the potential increase in dynamics of Na2 and Ha with temperature is not noticeable. However, the data indicate a slightly increased mobility of the hydride sites Hb-c-d and of the sodium ion Na1/Na3. More studies will be necessary to identify the most mobile ion.

Lastly, some attempts at introducing defects to increase ionic conductivity were attempted. For these attempts, divalent cations were to replace the sodium ion in Na_3SO_4H with the theoretical formula $Na_{3-2x}M_xSO_4H$ (M: Mg^{2+}, Ca^{2+}). The XRD measurements of the doped samples showed the appearance of new unidentified peaks (not corresponding to precursor peaks) and some changes in intensities of the existing peaks, suggesting unsuccessful doping. Furthermore, the conductivity measurements resulted in lower conductivity values, therefore these studies were concluded.

4. Conclusion

The sodium-rich anti-perovskite Na_3SO_4H which crystallizes in the *P*4/*nmm* space group was reproduced from literature with the first reports of its electrochemical properties reported in this work. The structural characterization relates closely to that performed by neutron powder diffraction. Thermal measurements do not show any phase transition below 623 K and show hydrogen release beginning at 633 K. To understand the electrochemical properties, EIS and DC measurements were performed in which the conductivity was 4.0×10^{-7} S/cm at room temperature. Further investigation of the electrochemical behavior by DC measurements was performed to understand the temperature evolution of conductivity with a room temperature electronic conductivity of 4.4×10^{-8} S/cm. Furthermore, solid-state ^{1}H and ^{23}Na high-resolution MAS-NMR revealed more complex sodium and hydrogen environments in Na_3SO_4H, with hydride defects that may influence ionic conduction. The MAS-NMR spectra were measured up to 423 K and demonstrated a limited evolution of the lineshapes for hydride defects and for the Na1(4e) site.

Funding
This work was co-funded by CNRS – France and by the Umicore Company.
Financial support from the IR INFRANALYTICS FR2054 for conducting the research is gratefully acknowledged. Dr. Franck Fayon (CNRS-CEMHTI) is acknowledged for insightful discussions.

Declaration of Competing Interest
The authors declare that they have no known competing financial interests or personal relationships that could have appeared to influence the work reported in this paper

References

[1] J. Janek, W.G. Zeier, A solid future for battery development, Nat. Energy. 1 (2016) 16141. https://doi.org/10.1038/nenergy.2016.141.

[2] Y. Zhao, L.L. Daemen, Superionic conductivity in lithium-rich anti-perovskites, J. Am. Chem. Soc. 134 (2012) 15042–15047. https://doi.org/10.1021/ja305709z.

[3] W. Xia, Y.Y. Zhao, F. Zhao, K. Adair, R. Zhao, S. Li, R. Zou, Y.Y. Zhao, X. Sun, Antiperovskite Electrolytes for Solid-State Batteries, Chem. Rev. 122 (2022) 3763–3819. https://doi.org/10.1021/acs.chemrev.1c00594.

[4] Z. Deng, D. Ni, D. Chen, Y. Bian, S. Li, Z. Wang, Y. Zhao, Anti-perovskite materials for energy storage batteries , InfoMat. (2021) 1–23. https://doi.org/10.1002/inf2.12252.

[5] J.A. Dawson, T. Famprikis, K.E. Johnston, Anti-perovskites for solid-state batteries: recent developments, current challenges and future prospects, J. Mater. Chem. A. (2021). https://doi.org/10.1039/d1ta03680g.

[6] P. Hartwig, A. Rabenau, W. Weppner, Lithium hydroxide halides: phase equilibria and ionic conductivities, J. Less-Common Met. 78 (1981) 227–233. https://doi.org/10.1016/0022-5088(81)90132-6.

[7] S. V. Krivovichev, Minerals with antiperovskite structure: A review, Zeitschrift Fur Krist. 223 (2008) 109−113. https://doi.org/10.1524/zkri.2008.0008.

[8] K. Kim, D.J. Siegel, Correlating lattice distortions, ion migration barriers, and stability in solid electrolytes, J. Mater. Chem. A. 7 (2019) 3216−3227. https://doi.org/10.1039/C8TA10989C.

[9] Y. Yu, Z. Wang, G. Shao, Theoretical formulation of Na3AO4X (A = S/Se, X = F/Cl) as high-performance solid electrolytes for all-solid-state sodium batteries, J. Mater. Chem. A. 7 (2019) 21985−21996. https://doi.org/10.1039/c9ta08584j.

[10] Z. Wang, H. Xu, M. Xuan, G. Shao, From anti-perovskite to double anti-perovskite: Tuning lattice chemistry to achieve super-fast Li+ transport in cubic solid lithium halogen-chalcogenides, J. Mater. Chem. A. 6 (2017) 73−83. https://doi.org/10.1039/c7ta08698a.

[11] Y. Yu, Z. Wang, G. Shao, Theoretical design of double anti-perovskite Na6SOI2 as a super-fast ion conductor for solid Na+ ion batteries, J. Mater. Chem. A. 6 (2018) 19843−19852. https://doi.org/10.1039/c8ta08412b.

[12] U. Rani, Y. Soni, P.K. Kamlesh, S. Pachori, A.S. Verma, Fundamental theoretical design of Na-ion and K-ion based double antiperovskite X6SOA2 (X = Na, K; A = Cl, Br and I) halides: Potential candidate for energy storage and harvester, Int. J. Energy Res. (2021) 1−19. https://doi.org/10.1002/er.6673.

[13] M.H. Braga, J.A. Ferreira, V. Stockhausen, J.E. Oliveira, A. El-Azab, Novel Li3ClO based glasses with superionic properties for lithium batteries, J. Mater. Chem. A. 2 (2014) 5470−5480. https://doi.org/10.1039/c3ta15087a.

[14] J.B. Goodenough, M.H. Braga, Batteries for electric road vehicles, Dalt. Trans. (2017). https://doi.org/10.1039/C7DT03026F.

[15] Y. Li, W. Zhou, S. Xin, S. Li, J. Zhu, X. Lü, Z. Cui, Q. Jia, J. Zhou, Y. Zhao, J.B. Goodenough, Fluorine-Doped Antiperovskite Electrolyte for All-Solid-State Lithium-Ion Batteries, Angew. Chemie Int. Ed. 55 (2016) 9965−9968. https://doi.org/10.1002/anie.201604554.

[16] K. Kim, Y. Li, P. Tsai, F. Wang, S. Son, Y. Chiang, D.J. Siegel, Exploring the Synthesis of Alkali Metal Anti-perovskites, Chem. Mater. 34 (2022) 947−958. https://doi.org/10.1021/acs.chemmater.1c02150.

[17] F. Wang, H.A. Evans, K. Kim, L. Yin, Y. Li, P.C. Tsai, J. Liu, S.H. Lapidus, C.M. Brown, D.J. Siegel, Y.M. Chiang, Dynamics of Hydroxyl Anions Promotes Lithium Ion Conduction in Antiperovskite Li2OHCl, Chem. Mater. 32 (2020) 8481−8491. https://doi.org/10.1021/acs.chemmater.0c02602.

[18] U.S Geological Survey, Mineral commodity summary - Lithium carbonate, U.S Geol. Surv. (2012).

[19] U.S Geological Survey, Mineral commodity summary - Lithium carbonate, U.S Geol. Surv. (2022).

[20] W.L. Bragg, C. Gottfried, J. West, The Structure of β Alumina ., Zeitschrift Für Krist. - Cryst. Mater. 77 (1930) 255−274. https://doi.org/https://doi.org/10.1524/zkri.1931.77.1.255.

[21] L.O. Hagman, P. Kierkegaard, The Crystal Structure of NaMe2IV(PO4)3; MeiV = Ge, Ti, Zr, Acta Chem. Scand. 22 (1968) 1822−1832.

[22] J.B. Goodenough, H.Y.P. Hong, J.A. Kafalas, Fast Na+ - Ion Transport in Skeleton Structures, 11 (1976) 203−220. https://doi.org/https://doi.org/10.1016/0025-5408(76)90077-5.

[23] H.Y.P. Hong, Crystal structures and crystal chemistry in the system Na1+xZr2SixP3-xO12, Mater. Res. Bull. 11 (1976) 173−182. https://doi.org/10.1016/0025-5408(76)90073-8.

[24] M. Jansen, U. Henseler, Synthesis, structure determination, and ionic conductivity of sodium tetrathiophosphate, J. Solid State Chem. 99 (1992) 110−119. https://doi.org/10.1016/0022-4596(92)90295-7.

[25] T. Krauskopf, S.P. Culver, W.G. Zeier, Local Tetragonal Structure of the Cubic Superionic Conductor Na3PS4, Inorg. Chem. 57 (2018) 4739−4744. https://doi.org/10.1021/acs.inorgchem.8b00458.

[26] Z. Zhang, Y. Shao, B. Lotsch, Y.S. Hu, H. Li, J. Janek, L.F. Nazar, C.W. Nan, J. Maier, M. Armand, L. Chen, New horizons for inorganic solid state ion conductors, Energy Environ. Sci. 11 (2018) 1945−1976. https://doi.org/10.1039/c8ee01053f.

[27] A. Mutschke, G.M. Bernard, M. Bertmer, A.J. Karttunen, C. Ritter, V.K. Michaelis, N. Kunkel, Na 3 SO 4 H─The First Representative of the Material Class of Sulfate Hydrides, Angew. Chemie Int. Ed. 60 (2021) 5683−5687. https://doi.org/10.1002/anie.202016582.

[28] S. Gao, T. Broux, S. Fujii, C. Tassel, K. Yamamoto, Y. Xiao, I. Oikawa, H. Takamura, H. Ubukata, Y. Watanabe, K. Fujii, M. Yashima, A. Kuwabara, Y. Uchimoto, H. Kageyama, Hydride-based antiperovskites with soft anionic sublattices as fast alkali ionic conductors, Nat. Commun. (2021) 1−10. https://doi.org/10.1038/s41467-020-20370-2.

[29] S. Fan, M. Lei, H. Wu, J. Hu, C. Yin, T. Liang, C. Li, A Na-rich fluorinated sulfate anti-perovskite with dual doping as solid electrolyte for Na metal solid state batteries, Energy Storage Mater. 31 (2020) 87–94. https://doi.org/10.1016/j.ensm.2020.05.030.

[30] J.B. Leriche, S. Hamelet, J. Shu, M. Morcrette, C. Masquelier, G. Ouvrard, M. Zerrouki, P. Soudan, S. Belin, E. Elkaïm, F. Baudelet, An Electrochemical Cell for Operando Study of Lithium Batteries Using Synchrotron Radiation, J. Electrochem. Soc. 157 (2010) A606. https://doi.org/10.1149/1.3355977.

[31] J. Rodriguez-Carvajal, FULLPROF: A Program for Rietveld Refinement and Pattern Matching Analysis, in: Abstr. Satell. Meet. Powder Diffr. XV Congr. IUCr, Toulouse, France, 1990: p. 127.

[32] D. Massiot, F. Fayon, M. Capron, I. King, L. Calv, B. Alonso, J. Durand, B. Bujoli, Z. Gan, G. Hoatson, Modelling one- and two-dimensional solid-state NMR, Magn. Reson. Chem. 40 (2002) 70–76. https://doi.org/10.1002/mrc.984.

[33] V.M. Goldschmidt, Die Gesetze der Krystallochemie, Naturwissenschaften. 14 (1926) 477–485. https://doi.org/10.1007/BF01507527.

[34] R.D. Shannon, Revised Effective Ionic Radii and Systematic Studies of Interatomie Distances in Halides and Chaleogenides, Acta Crystallogr. 32 (1976) 751–767. https://doi.org/10.1107/s0567739476001551.

[35] P.F. Lang, B.C. Smith, Ionic radii for Group 1 and Group 2 halide , hydride , fluoride , oxide , sulfide , selenide and telluride crystals, (2010) 7786–7791. https://doi.org/10.1039/c0dt00401d.

[36] Z. Zhang, L.F. Nazar, Exploiting the paddle-wheel mechanism for the design of fast ion conductors, Nat. Rev. Mater. 7 (2022) 389–405. https://doi.org/10.1038/s41578-021-00401-0.

[37] J.A. Dawson, H. Chen, M. Saiful Islam, Composition Screening of Lithium- and Sodium-Rich Anti-Perovskites for Fast-Conducting Solid Electrolytes, J. Phys. Chem. C. 122 (2018) 23978–23984. https://doi.org/10.1021/acs.jpcc.8b08208.

[38] E. Ahiavi, J.A. Dawson, U. Kudu, M. Courty, M.S. Islam, O. Clemens, C. Masquelier, T. Famprikis, Mechanochemical synthesis and ion transport properties of Na3OX (X = Cl, Br, I and BH4) antiperovskite solid electrolytes, J. Power Sources. 471 (2020) 228489. https://doi.org/10.1016/j.jpowsour.2020.228489.

[39] T. Famprikis, O.U. Kudu, J.A. Dawson, P. Canepa, F. Fauth, E. Suard, M. Zbiri, D. Dambournet, O.J. Borkiewicz, H. Bouyanfif, S.P. Emge, S. Cretu, J.N. Chotard, C.P. Grey, W.G. Zeier, M.S. Islam, C. Masquelier, Under pressure: Mechanochemical effects on structure and ion conduction in the sodium-ion solid electrolyte Na3PS4, J. Am. Chem. Soc. 142 (2020) 18422–18436. https://doi.org/10.1021/jacs.0c06668.

[40] Ö.U. Kudu, T. Famprikis, B. Fleutot, M.D. Braida, T. Le Mercier, M.S. Islam, C. Masquelier, A review of structural properties and synthesis methods of solid electrolyte materials in the Li2S − P2S5 binary system, J. Power Sources. 407 (2018) 31–43. https://doi.org/10.1016/j.jpowsour.2018.10.037.

[41] P. Gorai, T. Famprikis, B. Singh, V. Stevanović, P. Canepa, Devil is in the Defects: Electronic Conductivity in Solid Electrolytes, Chem. Mater. 33 (2021) 7484–7498. https://doi.org/10.1021/acs.chemmater.1c02345.

[42] T. Famprikis, P. Canepa, J.A. Dawson, M.S. Islam, C. Masquelier, Fundamentals of inorganic solid-state electrolytes for batteries, Nat. Mater. 18 (2019) 1278–1291. https://doi.org/10.1038/s41563-019-0431-3.

[43] F. Han, A.S. Westover, J. Yue, X. Fan, F. Wang, M. Chi, D.N. Leonard, N.J. Dudney, H. Wang, C. Wang, High electronic conductivity as the origin of lithium dendrite formation within solid electrolytes, Nat. Energy. (2019). https://doi.org/10.1038/s41560-018-0312-z.

[44] S.J. Turrell, H.J. Lee, M. Siniscalchi, S. Narayanan, M. Pasta, S.C. Speller, C.R.M. Grovenor, Fabrication of thin solid electrolytes containing a small volume of an Li3OCl-type antiperovskite phase by RF magnetron sputtering, Mater. Adv. 3 (2022) 8995–9008. https://doi.org/10.1039/d2ma00971d.